The Astrophysical Journal Supplement Series, 249:28 (10pp), 2020 August https://doi.org/10.3847/1538-4365/ab9eba

Magnetic Field Dropouts at Near-Sun Switchback Boundaries: A Superposed Epoch Analysis

W. M. Farrell[1], R. J. MacDowall[1], J. R. Gruesbeck[1], S. D. Bale[2,3], and J. C. Kasper[4,5]
[1] Solar System Exploration Division, NASA/Goddard Space Flight Center, Greenbelt, MD, USA
[2] Space Science Laboratory, University of California, Berkeley, CA, USA
[3] Physics Department, University of California, Berkeley, CA, USA
[4] Climate and Space Sciences and Engineering, Univ. of Michigan, Ann Arbor, MI, USA
[5] Smithsonian Astrophysical Observatory, Cambridge, MA 062220, USA
Received 2020 May 12; revised 2020 June 8; accepted 2020 June 16; published 2020 August 5

Abstract

During Parker Solar Probe's first close encounter with the Sun in early 2018 November, a large number of impulsive rotations in the magnetic field were detected within 50 R_s; these also occurred in association with short-lived impulsive solar wind bursts in speed. These impulsive features are now called "switchback" events. We examined a set of these switchbacks where the boundary transition into and out of the switchback was abrupt, with fast B rotations and simultaneous solar wind speed changes occurring on timescales of less than ~10 s; these thus appear as step function-like changes in the radial component of B and V. Our objective was to search for any diamagnetic effects that might occur especially if the boundaries are associated with quick changes in density (i.e., a steep spatial density gradient at the switchback boundary). We identified 25 switchback entries where the radial component of B, B_r, quickly transitioned from large negative to positive values and V_r simultaneously abruptly increased (i.e., step-up transitions) and 28 switchback exits where B_r quickly transitioned from large positive to negative values and V_r simultaneously abruptly decreased (i.e., step-down transitions). We then performed a superposed epoch analysis on each of these sets of events. We found these fast-transitioning events typically had a clear and distinct decrease in the magnetic field magnitude by 7%–8% detected exactly at the boundary. The presence of the $|B|$ dropout suggests there is a diamagnetic current present at the boundary.

Unified Astronomy Thesaurus concepts: The Sun (1693); Solar wind (1534); Solar physics (1476)

1. Introduction

A new era in solar exploration was initiated on 2018 August 12 with the launch of Parker Solar Probe (hereafter Parker). This spacecraft was specifically designed to make a series of close approaches to the Sun—including sampling for a short period near 10 R_s (Fox et al. 2016)—with state-of-the-art magneto-plasma, energetic particle, and sensitive imaging systems. The primary objectives of the mission are to understand the flow of energy into the corona; ascertain the structure, dynamics, and acceleration processes for the solar wind; and garner new insights into the processes that are responsible for solar energetic particles (Fox et al. 2016). Given these objectives, the spacecraft includes four unique investigations to measure the near-Sun space environment, including the FIELDS investigation to measure electric fields, magnetic fields, and associated plasma waves (Bale et al. 2016); the Solar Wind Electron, Alpha, and Proton (SWEAP) investigation to measure solar wind plasma characteristics (Kasper et al. 2016); the Integrated Science Investigation of the Sun investigation to measure solar energetic ions and electrons properties (McComas et al. 2016); and the Wide-field Imager for Solar Probe Plus investigation to image faint solar wind plasma structures in the inner heliosphere (Vourlidas et al. 2016). Herein, we focus on FIELDS and SWEAP measurements obtained from Parker's first close encounter ($E1$) with the Sun having a closest approach on 03:37 UT on 2018 November 6 at <36 Rs.

Bale et al. (2019) and Kasper et al. (2019) describe initial results found during this early Parker encounter. A number of expected features were detected during the Parker inbound and outbound period including a B-field magnitude that varied with heliocentric distance as $1/r^2$ (Bale et al. 2019). The solar wind speed also developed an overall stronger rotational component to its flow as Parker probed inward (see Figure 4 of Kasper et al. 2019). There was also the detection of current sheet crossings beyond 50 R_s that could be predicted and understood in the context of existing solar magnetic models and at least one passing coronal mass ejection was also detected within 100 R_s (see Figure 1 of Bale et al. 2019). In the near-encounter period, Parker was moving in the transverse direction at a speed that was nearly at the solar corotation speed—and at closest approach spent considerable time magnetically connected to a coronal hole that was emitting relatively slow solar wind (Bale et al. 2019).

However, during the period of time Parker was within 50 R_s, an unanticipated feature was repeatedly observed: abrupt rotations in the magnetic field that were often accompanied by increases in the radial component of the proton velocity (Bale et al. 2019; Kasper et al. 2019). In some cases, the radial component of the magnetic field, B_r, almost completely reversed. Such events have similarities to those reported previously from the more-distant Helios and Ulysses spacecraft (Balogh et al. 1999; Horbury et al. 2018). However, in the Parker case, the sheer number and rapidity of these magnetic "switchback" events during the close encounter period was unanticipated/unexpected.

Horbury et al. (2020) reported that for the 4 day period around perihelion, over 2000 impulsive switchbacks were

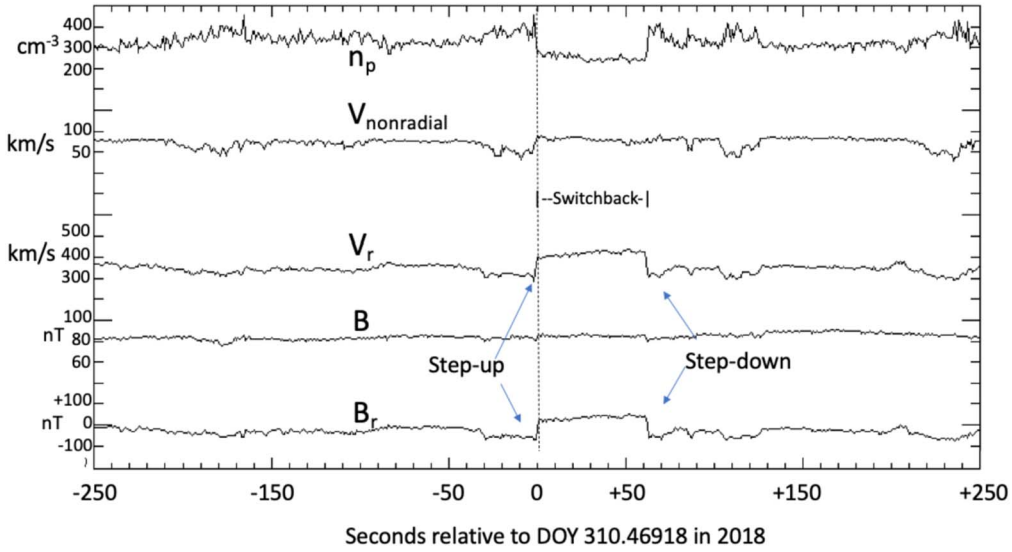

Figure 1. A switchback event with a step-like transition in B_r and V_r at the boundary of the feature. The analysis herein will focus on these abrupt switchback boundary transitions.

identified with typical durations in the tens of seconds and rotations ranging from 30° to 120°. The impulsive rotations were so numerous that their occurrence occupied 47% of the 4 day period. They surmised that the width of the switchbacks were of the order of 10^4 km and that the individual switchbacks are likely long and thin—"cigar shaped." They reported that individual events tended to cluster in episodes lasting hours but there were also periods of undisturbed, quiet Alfvénic slow solar wind interspersed between switchback episodes (e.g., Figure 2 of Bale et al. 2019). The switchback event duration and switchback-to-switchback wait times both followed power-law distributions (Chhiber et al. 2020; Dudok de Wit et al. 2020); thus there was not a specific frequency of occurrence and there was no single duration to the events (and event episodes). The switchbacks appear to have *B*-field topologies that differed from flux ropes (Zhou et al. 2020) and they were not considered to be reconnection events (Phan et al. 2020). Both the ion kinetic energy and Poynting flux were found to increase in the switchback events with the flow away from the Sun (Mozer et al. 2020). Models of the switchbacks suggest they are Alfvénic magnetic fluctuations that have developed S-like kinks in their magnetic field geometry (Kasper et al. 2019; Tenerani et al. 2020) possibly forming in association with normalized wave growth during fast outward magneto-plasma expansions (Squire et al. 2020).

Figure 1 shows Parker observations for a single switchback event that occurred near mid-day on 2018 November 6. Note that this specific event is characterized by an abrupt change in B_r (from negative to positive B_r values) and a simultaneous abrupt increase in V_r. The abruptness of the transition at a few seconds made them appear as step-like functions with a step-up in B_r and V_r upon entering into the switchback and a step-down upon exiting. In this study, we will identify those switchbacks with the most abrupt simultaneous changes in B_r and V_r. In the case in Figure 1, there was also a noticeable change in the nonradial component of *V* upon entry into the switchback and a corresponding simultaneous abrupt decrease in the proton density, n_p. Upon exiting, the density returns to pre-switchback levels.

In this work, we will specifically examine the boundary of the switchback events during encounter *E*1 as Parker enters and exits the features. Bale et al. (2019) reported that the switchback events early on 2018 November 5 possessed a rotation in *B* (i.e., B_r increased from negative to positive values), a V_r increase, an electron density increase, and a simultaneous magnetic magnitude decrease. The anticorrelation of density and |*B*|, which occurred abruptly at the boundary of the switchback, is suggestive of a possible pressure balance effect where B^2 would decrease with an increase in plasma density or even an added partial diamagnetic effect where *B* would vary around regions where there is a gradient in the density. We consider that the formation of *B*-field altering currents would be most intense at the boundaries where there are abrupt changes and thus strong gradients (e.g., fast change in both *B* and n). We thus perform a superposed epoch analysis on a set of boundaries that have sharp, near-discontinuous changes representing boundaries with the steepest gradients in B_r and V_r (i.e., the boundaries with near step function-like edges). As we report herein, our analysis of the specific switchbacks having sharp, step-like boundaries yields new results, especially regarding the relationship of density and |*B*| at the boundary crossings.

2. Measurement Set

The data set used was the high-level products online on the CDAWeb (https://cdaweb.gsfc.nasa.gov/index.html/). Specifically, high rate FIELDS *B*-field data in radial-tangential-normal (RTN) coordinates were obtained with four samples per instrument cycle. This data set was then decimated to 1 s intervals. Similarly, SWEAP high rate proton density and velocity moments in RTN coordinates were obtained and the data set was decimated to 1 s intervals. RTN coordinates are defined by a unit vector, *R*, in the radial direction outward from the Sun center to the spacecraft, a unit vector *T* defined by the cross product of the solar rotation axis with *R*, and unit vector *N* defined as orthogonal vector to these other two vectors. The description of FIELDS's magnetometer that acquired the *B*-field data set is found in Bale et al. (2016). The description of SWEAP's particle analyzers that obtained the n_p and velocity

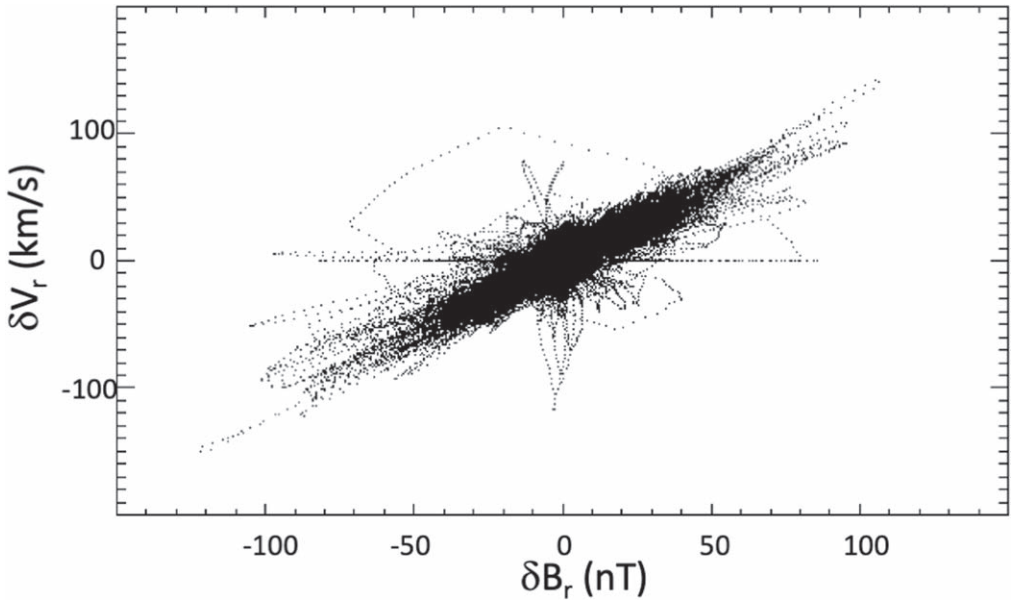

Figure 2. The distribution of δV_r vs. δB_r between 2018 DOY 308 and 312.

measurements is described in Kasper et al. (2016). The data set thus has fundamental variables: $|B|$, B_r, B_t, B_n, n_p, $|V|$, V_r, V_t, V_n, and $V_{nonradial} = (V_t^2 + V_n^2)^{1/2}$.

Besides these fundamental variables, we developed a set of derived quantities for use in both correlative and superposed epoch analysis studies. Since we are searching for abrupt step-like changes in the variables, especially B_r and V_r, we used the difference in values to identify quick variations. For example, we defined a derived variable δB_r where, at any instant in time, t_o, the average of the B_r values in the 30 s after t_o was subtracted from the average of the B_r values in the 30 s before t_o: $\delta B_r(t_o) = \langle B_r \rangle_{after} - \langle B_r \rangle_{before}$. Using this same approach for the fundamental variable set, we produced a set of derived quantities $\delta|B|$, δB_r, δB_t, δB_n, δn_p, $\delta|V|$, δV_r, δV_t, δV_n, and $\delta V_{nonradial}$ that were used to identify abrupt changes in the variables. While we applied a 30 s window, we also ran 5 s and 100 s windows and the trends described below were nearly identical to the 30 s results.

Regarding the δ quantities, the spacecraft was moving nearly 90 km s^{-1} in the T direction in the near-encounter period. The plasma is also erupting below Parker and immersing Parker in the faster switchback outflow along R. Thus, given a $\sim$300 km s^{-1} radial flow, a temporal scale of 30 s corresponds to a spatial scale of about 9000–10,000 km. Thus, the δ variables remains sensitive to changes in structures on the scale size of many 1000's of kilometers.

The nature of the δ analysis especially recognizes step-like changes in the variables that persist for 10's of seconds. For example, consider a change in B_r like that shown in Figure 1. Upon Parker's entry into the switchback at $t = 0$ s, the δB_r variable had a maximum value as the difference between $\langle B_r \rangle_{after}$ and $\langle B_r \rangle_{before}$ became $\sim +100\,nT$. Upon Parker's exit of the switchback near $t = +65$ s, the difference between $\langle B_r \rangle_{after}$ and $\langle B_r \rangle_{before}$ was less than $-100\,nT$. In contrast, in regions away from the switchback boundary, δB_r was small.

3. Correlative Analysis and SBI

Given the variable set, we then performed correlations of pairs in order to reveal trends in the data during periods of heavy switchback activity. For a correlation analysis, we selected a 4 day period centered around $E1$ closest approach: DOY 308–312 (2018 November 4–8). During this period, there were numerous switchback events where B quickly rotated and thus B_r abruptly changed from low negative values ($<50\,nT$) to positive values $B_r > 0$. We thus focus on the correlation of variables with δB_r. We plot the distribution of two simultaneously made observations over the 4 day period.

Figure 2 shows the distribution of δV_r versus δB_r for each second during the 4 day period with the distribution of measurements clearly indicating a very strong positive, linear relationship. We note that when we ran the same analysis at a later time without substantial switchback activity (DOY 319–323), δV_r versus δB_r had a slight negative relationship. Clearly, when there were abrupt changes in B_r, V_r also changed (e.g., Figure 1). When B_r exhibited a large positive step-like change upon entering switchbacks, V_r also increased in stepwise fashion. When B_r exhibited a large negative change upon exiting switchbacks, V_r also decreased simultaneously.

Figure 3 shows the distribution of δn_p versus δB_r for each second in the 4 day period. The distribution of points is more complex—indicative of two trends. First, there is a trend where n_p made substantial changes and B_r remained mostly unaffected —no change in B_r ($\delta B_r \sim 0$). This trend is evident by the vertical distribution of points (a vertical black line is used to aid the eye). However, there is a second trend, where the change in n_p occurs with an abrupt change in B_r (a tilted line is used to aid the eye). Note that as B_r makes abrupt, large positive swings, like at entries into switchbacks, n_p tends to decrease. When B_r makes large abrupt negative swings, like at switchback exits, n_p tends to increase. The plasma content appears to drop out within the switchbacks that have the largest δB_r values. This statistical trend is revealed in individual cases like that shown in Figure 1, where the density was found to decrease substantially within the sharp-edged switchback.

Figure 4 shows the distribution of $\delta|B|$ versus δB_r that indicates, for the most part, that there is not a strong correlation. Note that most of the points follow the horizontal line that indicates that $|B|$ is mostly unchanged with big changes

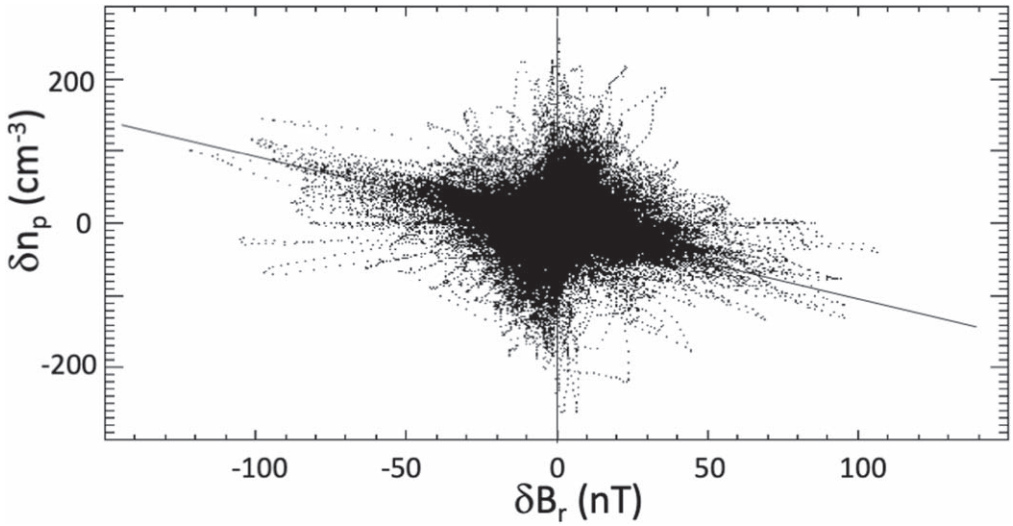

Figure 3. The distribution of $\delta n_{\rm p}$ vs. $\delta B_{\rm r}$ between 2018 DOY 308 and 312.

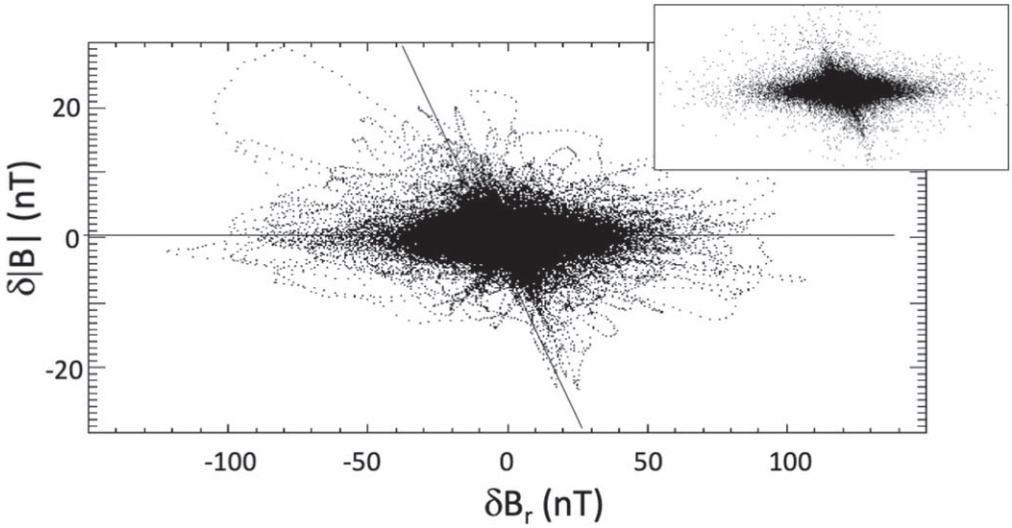

Figure 4. The distribution of $\delta|B|$ vs. $\delta B_{\rm r}$ between 2018 DOY 308 and 312. The inset shows the same δ analysis now run for a case where δ differences are taken over 5 s, as opposed to 30 s.

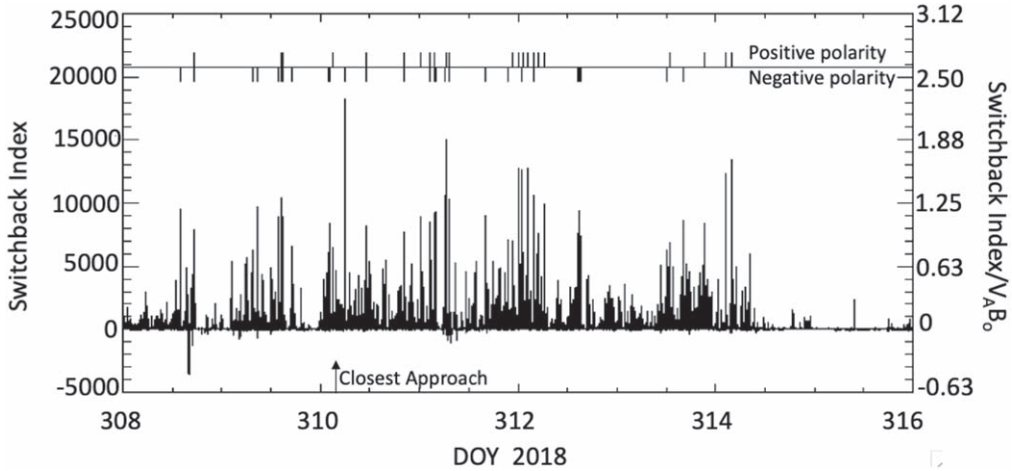

Figure 5. The SBI during $E1$. The index identified those switchback boundaries with the most abrupt simultaneous change in both $B_{\rm r}$ and $V_{\rm r}$. The line at the top indicates the time and polarity (step-up or step-down) for those specific boundary crossings that have a SBI of $>6000\,nT\,{\rm km\,s^{-1}}$. The right-hand side shows the normalized SBI with $V_{\rm A} = 300\ {\rm km\ s^{-1}}$ and $B_{\rm o} = 80\,nT$.

in B_r. However, there is evidence for a small set of points that suggest that $|B|$ decreases with abrupt changes in B_r (the tilted line is drawn to aid the eye).

To resolve this possible trend, we re-ran our δ analysis now changing the averaging time window between points to 5 s (rather than 30 s as originally run) and the result is displayed in the inset. The $\delta|B|$ versus δB_r correlation reveals itself more clearly when considering a quicker change and suggests there is evidence for an impulsive change in B magnitude when there is an abrupt change in B_r. We will elaborate more on a possible quick change in $|B|$ in association with a change in B_r when describing the superposed epoch analysis results.

To explore these trends near the boundary of the switchbacks, we are in need of some method to identify the sharp-edged boundaries in a systematic way. As evident in Figure 2, when there is an abrupt change in B_r, the variable V_r will also abruptly change at the switchback boundary. Thus, a possible index to identify steep switchback edges is $\delta B_r \cdot \delta V_r$.

From Figure 3, given that density also changes with δB_r, another possible index is $-\delta n_p \cdot \delta B_r \cdot \delta V_r$. An advantage of this index is that it would also give the polarity of the change (a step-up at switchback entry being positive and step-down at switchback exit being negative). However, as indicated in Figure 3, abrupt changes in n_p occur independent of the switchbacks and there is the potential to create a false identification of boundaries, especially for the ill-resolved boundaries.

We thus define a switchback index (SBI) as $\delta B_r \cdot \delta V_r$ that then allows a unique identification of the most abrupt switchback boundaries. This index would key in on the step-like changes, like those occurring at the boundary of the switchback in Figure 1. The polarity of the switchback edge (step-up versus step-down) is then indicated by $\delta B_r/|\delta B_r|$ and the SBI can be multiplied by this polarity function to provide the identification of events having the most abrupt changes upon entering (step-up) or exiting (step-down) the switchback.

Figure 5 shows the SBI for the time period near $E1$ closest approach. The SBI has a large number of high valued events that are in association with the abrupt changes in both B_r and V_r that occur at the numerous switchback edges. If we consider the boundary crossings having the largest SBI, i.e., those exceeding $6000\,nT\,\mathrm{km\,s^{-1}}$, there are 25 positive-polarity boundaries (step-up at the entry) and 28 negative polarity boundaries (step-down at the exit). The time and polarity of these strongest events are indicated at the top of Figure 5.

We note that the SBI is not normalized but can be normalized by dividing the SBI by the Alfvén speed ($\sim$100 $\mathrm{km\,s^{-1}}$ for an 80 nT B field and 300 $\mathrm{cm^{-3}}$ proton density) and magnetic field (80 nT) during the closest approach period of Encounter 1. This normalized SBI is included on the right-hand side of the Figure 5. The normalized quantity reveals the extreme nature of the abrupt changes at the switchback boundaries.

4. Superposed Epoch Analysis

Given that the SBI can provide the timing of the step-like switchback boundaries, these fast-changing boundaries can be examined as a group to derive their properties. Specifically, we performed a superposed epoch analysis on the set of 25 positive-polarity boundaries having SBI values exceeding $6000\,nT\,\mathrm{km\,s^{-1}}$. Measurements from a period of time 250 s before and after the boundary were co-added to identify any subtle, repeating feature at the crossings.

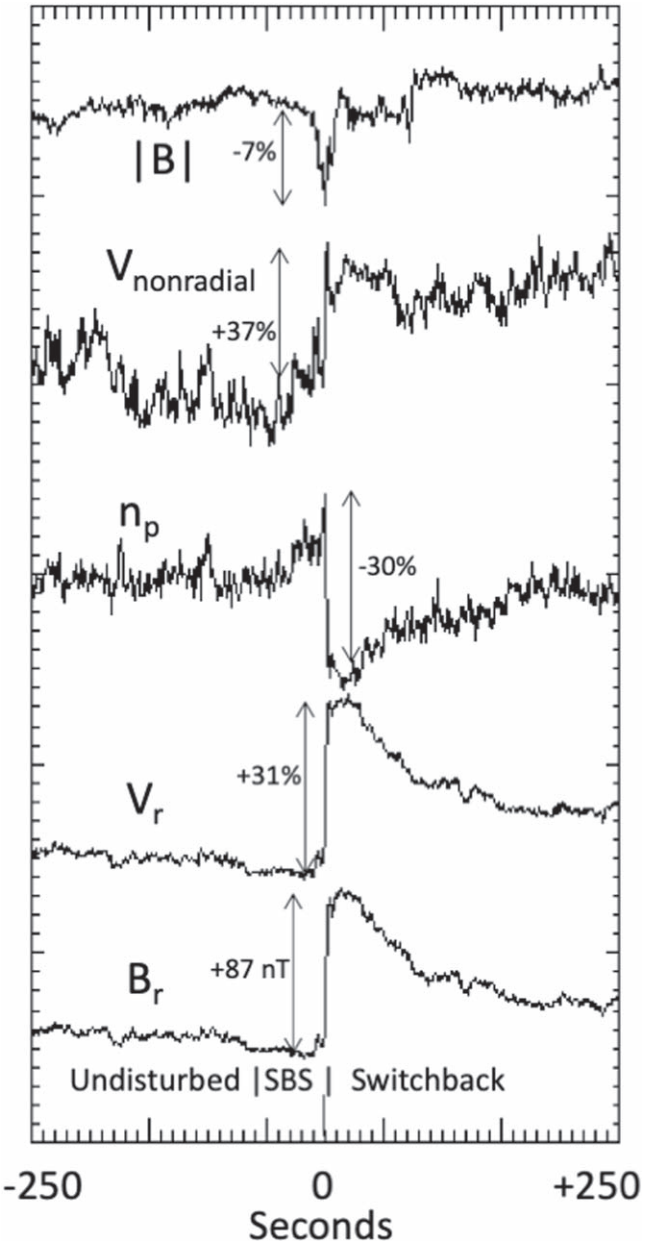

Figure 6. The superposed epoch analysis over the 25 boundaries possessing step-up changes. "0" s represents the time of the boundary crossing as identified by the SBI and every time tick is 10 s.

Figure 6 shows the results of the analysis from co-adding the 25 events possessing positive (step-up) boundaries. The B_r profile at the bottom of the figure was directly co-added and divided by the number of events. On average, there was a change in the B_r value of about 87 nT for these 25 events. The large change in B_r, which is nearly comparable to the magnitude $|B|$, indicates that these events underwent substantial rotation. The other four profiles in the figure are the results of co-adding of relative values; for each of the 25 crossings, an average value for each variable was derived in the first 240 s (-250 s to -10 s) prior to crossing into the switchback. The variable values in all 500 s were then subtracted from this average and then divided by this average. The relative values for each event were then co-added in time. This normalization

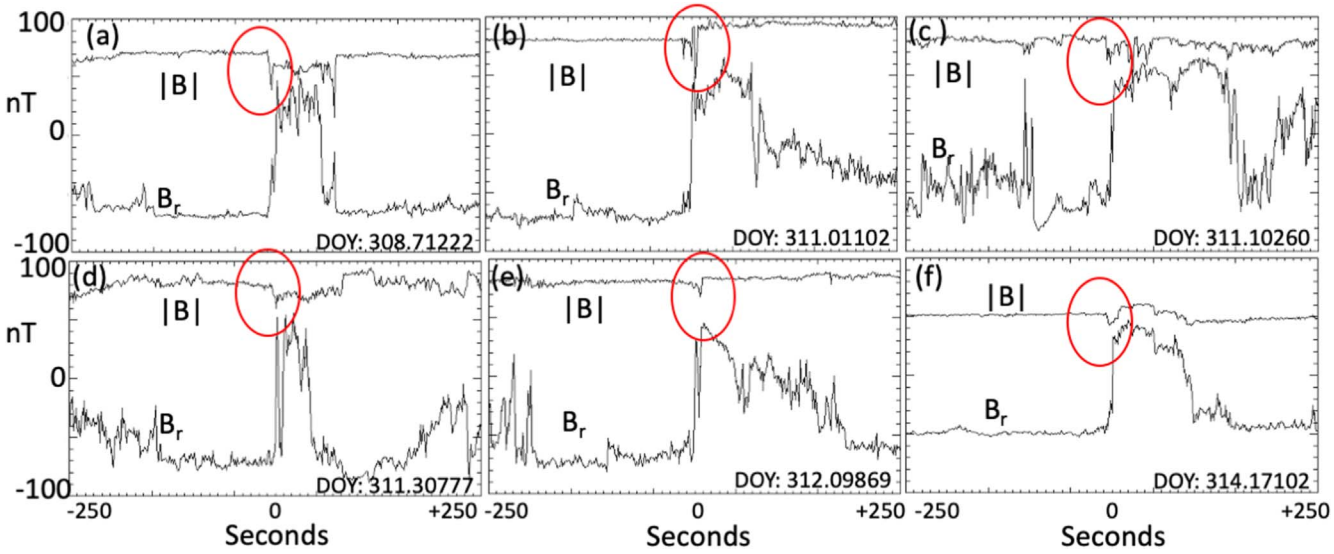

Figure 7. Six examples of the dropout in $|B|$ from the set of 25 positive polarity switchback crosssings used in the superposed epoch analysis. The red circle identifies the local minimum in $|B|$ found at the boundary crossing.

allows all crossings to be weighed equally and avoids the superposed epoch analysis from being overweighted by a few events having larger values.

There are some notable features of the analysis. First, both B_r and V_r have very clear and distinct changes across the boundary, as would be anticipated given the index used to identify the boundary is defined by the large, abrupt changes in B_r and V_r. After about 40 s following the boundary crossing, the co-added B_r and V_r values begin to decay in time, suggesting that Parker has exited some number of the switchbacks. In essence, the decay in V_r and B_r provides a statistical event duration of the 25 switchbacks—and that half-width duration is about 70 s. This nominal duration is similar to that reported previously by Horbury et al. (2020). Dudok de Wit et al. (2020) reported that the overall statistics of the switchback durations had a power-law distribution. In our case, we are looking at the 25–28 events having the quick, large B rotations and large simultaneous velocity changes. Our smaller population of events very likely resides in the tail of Figure 6 of Dudok de Wit et al. (2020). Thus, our quoted durations are a result of a selection effect (we are selecting for large $\delta B_r \cdot \delta V_r$) and do not negate the Dudok de Wit et al. (2020) result that examined duration (residency) time for all events.

We find there is a very strong correlation of the co-added profiles of B_r and V_r with the two profiles in Figure 6 sharing features even in regions away from the boundary. For example, both profiles have a local minima about +120 s. They also have a local maxima at +210 s. This result is consistent with Figure 2, which also revealed the very direct connection between the two variables even at small δB_r and δV_r values. These two variables appear to track each other very closely in and around these sharp-edged switchbacks.

We also note the presence in the co-added profiles of B_r and V_r of a possible precursor layer—a switchback sheath—just prior to entry across the boundary (labeled switchback sheath, or SBS, in Figure 6). This region appears in the profiles between −60 s and 0 s where both B_r and V_r values become depressed relative to the nominal, undisturbed values between −250 and −60 s. Note that the density also slightly increases during this same time, having values progressively increasing above those found at earlier times between −250 and −60 s. $|B|$ also begins a period of steadily decreasing values in the SBS time (although the signature in $|B|$ is not as obvious). The individual switchback in Figure 1 also shows evidence of this SBS, including a relative increase in n_p, at the switchback entry and exit.

Upon crossing the boundary, the density has an abrupt drop in value, being reduced by almost 30% relative to pre-boundary values. Also, the nonradial solar wind flow undergoes a systematic deflection by 37% at the boundary. The density profile possesses a peak right at the boundary itself; this is a real effect. There are a number of crossings where n_p possesses an isolated spike in values. This spike does not occur on every crossing but occurs in a number of cases to thus become a co-added feature in the superposed analysis. For example, an isolated density maxima (i.e., spike) was detected at the switchback entry ($t = 0$ s) in the case shown in Figure 1.

However, a most stunning feature of the analysis is the clear and distinct dropout in $|B|$ occurring at the boundary crossing, with a relative decrease of 7% compared to pre-boundary values. The co-added B-field magnitude across the set of 25 events is actually unchanged deeper in the switchback compared to pre-boundary values, reflecting the fact that $|B|$ in each case sometimes increases or decreases in the switchback compared to the pre-boundary values—and when co-added they sum to pre-boundary values. However, the $|B|$ boundary dropout appears to be a feature that occurs on many events that becomes resolved upon co-adding in time. This short-lived feature may be the source of the population of correlated $\delta|B|$ versus δB_r measurements found in the distribution shown in Figure 4. The population of correlated $\delta|B|$ versus δB_r measurements became more resolved when we decreased the averaging time interval, which is consistent with the short-lived nature of the $|B|$ dropout.

Figure 7 shows 6 individual positive (step-up) boundary crossing that make up the 25 cases used in the analysis. Both B_r and $|B|$ are shown. In these cases, the abrupt change in B_r is accompanied by a decrease in $|B|$ exactly at the transition (which, in this case, is centered at 0 s). The value of $|B|$ deeper within the switchback (where $B_r > 0$) is sometimes lower or

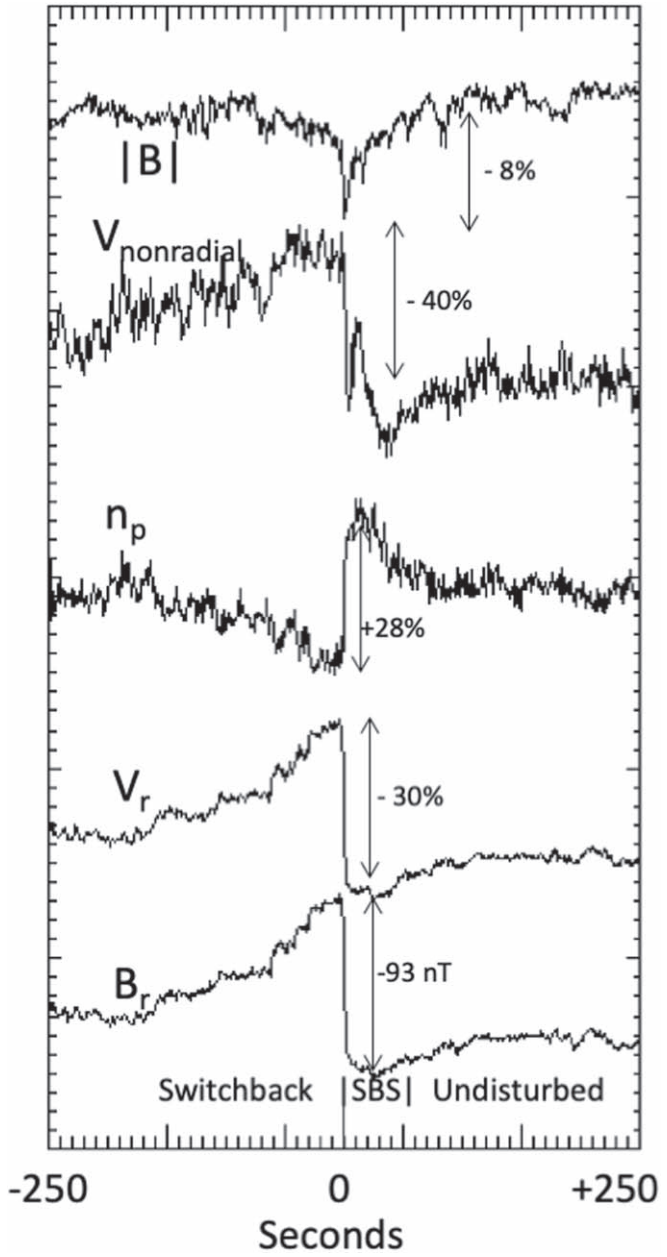

Figure 8. The superposed epoch analysis over the 28 boundaries possessing step-down changes. "0" s represents the time of the boundary crossing as identified by the SBI and every time tick is 10 s.

sometimes higher than $|B|$ outside the switchback. However, the local minimum in $|B|$ (i.e., the dropout) is an obvious feature (circled in red). Note that in panels (a), (c), (d), and (f), there is also a $|B|$ dropout upon exiting the switchback as well (at the negative polarity, step-down boundary).

Figure 8 show the superposed epoch analysis for the 28 switchback boundaries that have the most abrupt step-like decrease in both B_r and V_r. In these cases, the SBI is $>6000\,nT\,\mathrm{km\,s^{-1}}$ but the polarity is negative (see Figure 5) and these step-down cases are co-added in time, like in Figure 6. The one difference between the two cases is that the relative values for V_r, n_p, $V_{\mathrm{nonradial}}$, and $|B|$ in each crossing used in Figure 8 are calculated relative to the average value outside the switchback between +10 s to +250 s. Thus, in both Figures 6 and 8, the event average used to derive relative values was obtained in the region with undisturbed plasma outside the switchback. In Figure 6, the external region outside the switchback is between −250 s and −10 s for each event, and in Figure 8, the external region is between +10 s and +250 s for each event.

Complementary trends are seen in the negative polarity, step-down cases as in the positive-polarity, step-up cases. Specifically, upon exiting the switchback, both B_r and V_r displayed a substantial abrupt decrease. The trend was that B_r underwent a fast rotation back to $B_r < 0$ values as Parker exited the switchback. The density tended to increase by 28% upon exiting the switchbacks and there was, generally, a deflection in the nonradial flow at the boundary. Once again, $|B|$ displayed a statistically significant dropout of −8% right at the boundary itself. There is also evidence of an SBS found just after the exit from the boundary between 0 s and + 60 s, but this layer is not as obvious as in Figure 6. In this layer, the density again increases just outside the switchback and $|B|$ again steadily decreases from +60 s to 0 s, reaching its minimum at 0 s. Comparing both Figures 6 and 8, given that there is a tendency to observed this switchback sheath both at the entry and exit of the switchback, we suggest the sheath would then be a thin outer skin surrounding the larger "cigar-shaped" (Horbury et al. 2020) switchback structure.

5. Discussion and Conclusions

We performed a superposed epoch analysis on the switchback events possessing the most abrupt change in B_r and V_r in time, i.e., those switchback boundaries with step-like transitions. The superposed epoch analysis proved very revealing, resolving consistent features that are typically overlooked when examining single events due to the very dynamic nature of activity in and around the switchback.

We conclude that the sharpest switchback edges—those most like a step function—will tend to produce a clear and distinct decrease in $|B|$ at both the entry and exit of the switchback. We also find that the proton density decreased upon crossing into the switchback and reverted back to nominal levels upon exiting. However, there is evidence for an increase in density that exists in a sheath region surrounding the switchback and appears just prior to entering and just after exiting.

The density measurements are obtained from the SWEAP Solar Probe Cup. One possible reason for the density decrease is that the solar wind flow direction changed orientation upon crossing into the switchbacks, thereby reducing the flux into the cup. We note from Figures 6 and 8 that indeed $V_{\mathrm{nonradial}}$ changes across the boundary. However, we find that the ratio of $V_{\mathrm{nonradial}}/V_r$ stays quasi-constant across the switchback boundaries, at least in a statistical sense. Figure 9 shows superposed epoch analysis results of the ratio of $V_{\mathrm{nonradial}}/V_r$ for the (a) 25 positive (step-up) and (b) 28 negative (step-down) cases. As indicated in the figure, there is not a substantial change in the ratios when crossing the boundary, with ratios ranging between 0.15 and 0.2 for both the entry and exit of the switchback. Hence, in summing the events, we found there was no large systematic angular deflection in the flow direction relative to the radial direction with the flow vector remaining near 10° for the set of switchback events. We thus conclude that the changes in density at the switchback edges are likely not associated with large angular changes in the flow. In the future, we will compare the SWEAP proton densities to the FIELDS electron

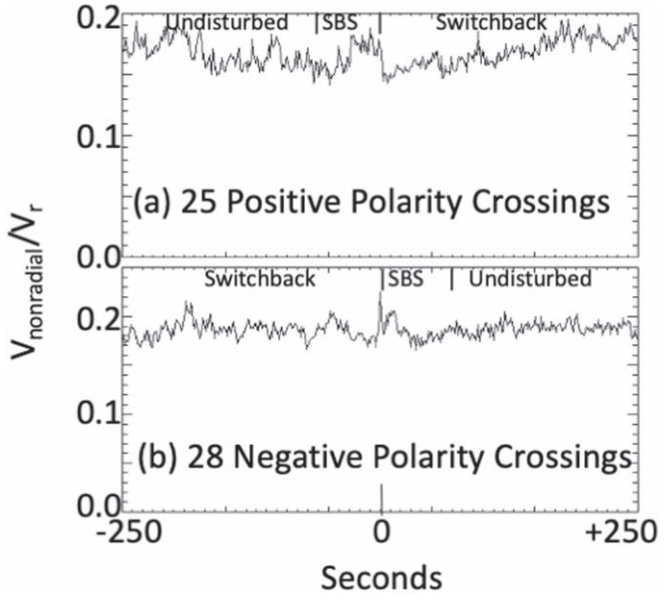

Figure 9. A superposed epoch analysis of the ratio of the nonradial-to-radial velocity flows for the set of (a) positive-polarity and (b) negative polarity switchback crossings.

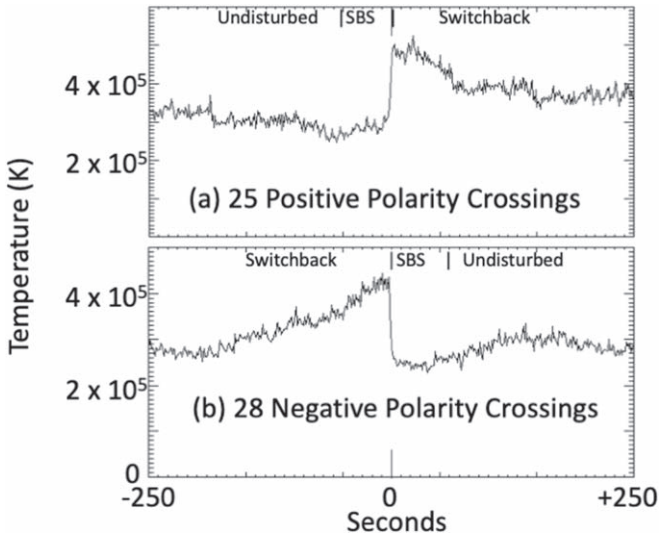

Figure 10. A superposed epoch analysis of the SWEAP ion temperature at the switchback boundaries.

densities derived via electron plasma frequency emission. However, merging those data sets is beyond the scope of this present work.

Figure 10 shows the results of the superposed epoch analysis for the SWEAP ion temperature for the (a) 25 positive (step-up) and (b) 28 negative (step-down) cases. The analysis for both types of boundary crossing shows a clear and distinct temperature increase in the switchback, by over 50%, with the change occurring abruptly at the boundary crossing. Thus, for the largest rotations of B that have the largest increase in V_r (i.e., greatest $\delta B_r \cdot \delta V_r$), the superposed epoch analysis also finds a statistical trend where there is also a simultaneous change in T_p. Kasper et al. (2019) initially reported on this ion thermal speed (i.e., temperature) increase at the switchback boundaries (see their Figure 2(b)). Mozer et al. (2020) also reported on this temperature increase, also occurring abruptly at

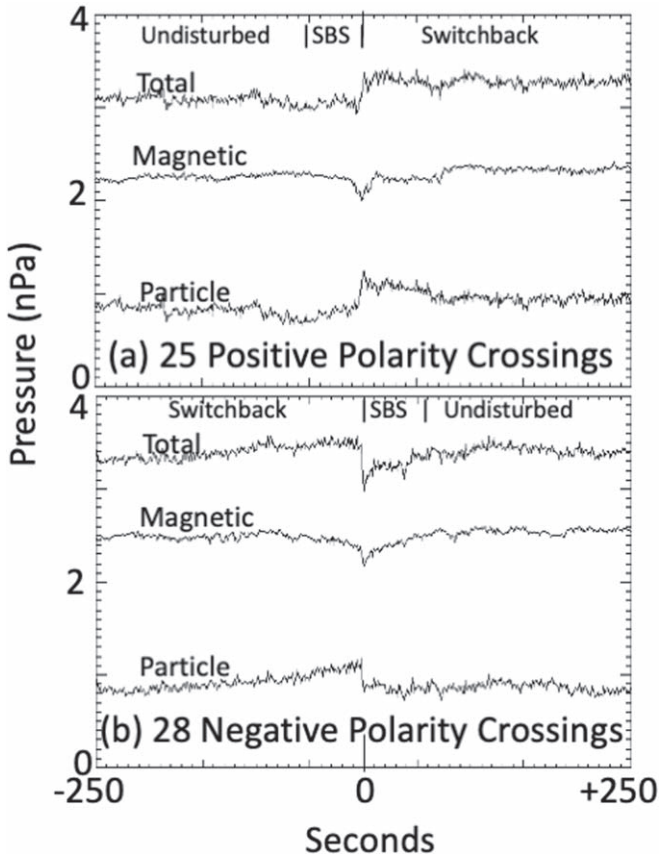

Figure 11. A superposed epoch analysis of the pressure at the switchback boundaries.

the boundary in their case (see their Figure 4(f)) and suggested that the warmer ions in the switchback are a possible result of magnetic microturbulence found within the switchbacks. This intriguing possibility would then connect the switchback evolution directly to the warmer plasma.

Combining the density, temperature, and $|B|$ values, we can then assess, in a statistical sense, the pressure across the boundary, where the thermal pressure is compared to the magnetic pressure. Figure 11 shows the superposed analysis for pressure using (a) the 25 positive-polarity (step-up) cases and (b) 28 negative polarity (step-down) cases. Note that the total of the thermal and magnetic pressure appears to be nearly balanced across the interface with a mild, but clear, discontinuity of ~10%–15% found at the boundaries. The change in pressure across the switchback exceeds the fluctuation level in the superposed analysis and thus is concluded to be a real effect. In case (a) (Parker switchback entries), the particle pressure increase has a local maximum right at the boundary and appears as the complement of the magnetic pressure decrease to thus almost be in balance. In case (b) (Parker switchback exits), there is again a local particle pressure maximum at the boundary, but the overall profile does not appear to be the complement of the magnetic pressure and an obvious discontinuity appears in the total pressure.

The overall pressure is greater within the switchback, which suggests that the region is possibly in the process of expanding. We suggest that the magnetoplasma in the switchback is possibly evolving to achieve a balance at larger radial distances. Future work will be to examine pressure balance for events found at larger distances for comparison.

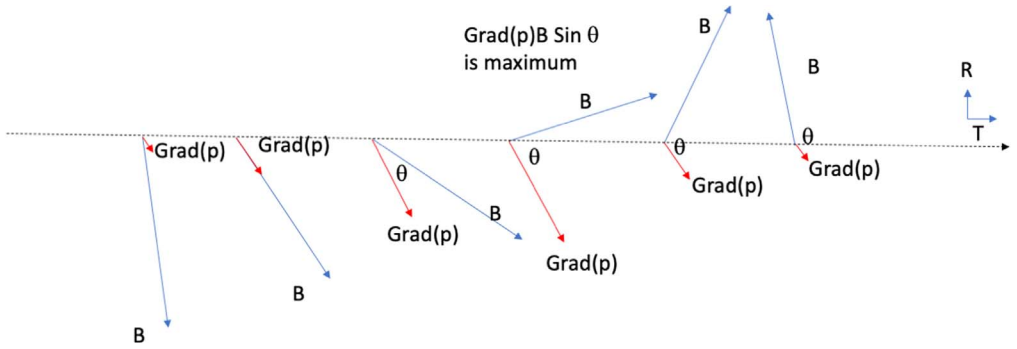

Figure 12. An illustration of the development of a diamagnetic current within the boundary in a situation where B quickly rotates relative to an intensifying spatial gradient in pressure.

Figures 6 and 8 both show evidence of a density dropout by ~30% within the switchbacks that were intercepted by Parker near 37 R_s. However, Horbury et al. (2018) reported no statistically significant density change within the set of Helios-detected switchbacks found near 62 R_s. These two observations, together, suggest that the plasma at the switchback edges might undergo expansion inward to fill in the density depletions as the voids propagate outward between 40 to 60 R_s. Such plasma expansions are well known to create anisotropies in the plasma flow that can give rise to a number of plasma wave modes that could act to heat the local proton population. While not a perfect analog, in the study of the plasma expansion at the lunar wake, expanding ions from one side of the density dropout were thought to interact with expanding ions from the opposite side of the dropout, creating an ion–ion counterflow that was found to be highly unstable (Ogilvie et al. 1996; Farrell et al. 1997, 1998). Such a situation might be occurring within the switchbacks. Future work includes examining the possibility of expansion, associated anisotropies, electrostatic wave activity, and plasma heating.

Regarding the precursor switchback sheath region, the region is not obvious at every crossing but appears in a large number of cases such as to be resolvable upon co-adding the large number of step-like boundary cases. While this statistical analysis does not reveal exactly why the sheath region forms, in general such regions are associated with backscattered/reflected electrons and ions from abrupt changes in B (and E) that form at boundaries. Future work includes a greater understanding of this switchback sheath region by examining more detailed electron and ion energy distributions, E-fields, and any plasma wave activity that might be indicative of a reflected component. For example, we note that V_r slows down in the sheath region, and this may be in association with ion–ion plasma instabilities that act to slow down the near-sheath solar wind via pickup of any boundary-reflected ion component. By flux conservation, the ion density then would be expected to increase giving rise to the larger ion density just prior to entry. Future work includes examining individual cases to understand how these variables are interconnected and to thus account for the sheath properties.

We also find that these sharp, well-defined switchback boundaries must contain a boundary current that flows in such a way as to cancel magnetic flux on either side of the switchback, thereby creating the $|B|$ dropout. Given the change in particle pressure upon crossing the boundary, a diamagnetic current is a likely candidate to be responsible for the dropout. However, diamagnetic currents proportional to $B\ x$ grad(p) are difficult to uniquely identify in this situation because we require knowledge of the spatial gradient in pressure (which we do not possess) and knowledge on how this gradient vector aligns in a B field that, itself, is quickly rotating across the boundary. If we assume that the pressure gradient vector remains steady across the boundary while B rotates (with θ representing the angle between the two vectors), there should be some location within the boundary where B grad(p) Sinθ is maximized as B rotates into a quasi-perpendicular geometry relative to grad(p). In essence, within the boundary, B rotates into a position where a diamagnetic current can be maximized (again, assuming a steady pressure gradient orientation across the boundary).

Figure 12 illustrates a possible nonunique scenario. In this case, the grad(p) vector maintains its approximate orientation but grows in magnitude across the boundary. During the crossing, B also rotates within the boundary. As B rotates, there is a location where $B\ x$ grad(p) is maximized and the diamagnetic current is at peak values. However, as B continues to rotate and grad(p) decreases, the diamagnetic currents reduce. In this illustration, the diamagnetic current (where the $|B|$ dropout is the deepest) points in the N direction and acts to reduce the B-field magnitude in the region to the left where $B_r < 0$ and in the region to the right where $B_r > 0$.

We can estimate the strength of this diamagnetic current using the particle pressure profile shown in Figure 11. The B-field perturbation created by an infinitely large current sheet is $\delta B = \mu_o\ j_d\ \delta s/2$, where δs is the thickness of the current sheet. The strength of the diamagnetic current is $|j_d| \sim$ grad(p)/B, which is approximately $\sim B^{-1}\ \delta p/\delta s$. Combining these two expressions allows us to derive the B-field perturbation from the diamagnetic current sheet as $\delta B \sim \mu_o\ \delta p/(2B)$. Figure 11 indicates that the statistically derived particle thermal pressure change at the switchback entry and exit is ~0.4 nPa, respectively. For $|B| \sim 90\,nT$, this corresponds to a $\delta B \sim 3nT$ or 3% deflection in the B field—a value similar to the measured B-field deflection. Hence, pressure-driven diamagnetic currents could be a source for the deflection in B. Using higher-resolution data, the gradient in pressure across the boundary might reveal even sharper changes than resolved herein (using 1 s data). Such a high-resolution data study of specific cases is beyond the scope of this current statistically based paper but will be carried out in the future.

Since the SBI is identifying those boundaries with the largest change in B_r, it is, by definition, also identifying boundaries that undergo the largest rotation in B. Thus, the boundaries used in the superposed epoch analysis herein will have the greatest likelihood of having a location somewhere within the

boundary where B grad(p) Sinθ is maximized. In other switchback boundaries that have small changes in B_r, the diamagnetic current may remain weak since B never rotates into a position to become quasi-perpendicular to the pressure gradient. In future work, one could use higher rate measurements of the rotating B at the boundary and the timing of the $|B|$ dropout (that is indicative of the location near the diamagnetic currents) to derive a range of vector positions of the spatial gradient in pressure.

Finally, we conclude that the boundary of the switchbacks, especially those with step-like changes, appears to be very complex. The presence of a switchback sheath including the possible proton density buildup at the switchback edges, along with the $|B|$ dropout, all suggest complex behavior at these boundaries. Comparing to Horbury et al. (2018), it also appears that the switchbacks are still evolving and thus undergoing processes that will eventually lead to density uniformity further out. Future work includes an examination of the electron and ion distributions that might reveal a diamagnetic flow as an anisotropy and plasma waves generated at the boundary that are indicative of anisotropic plasma populations. Clearly, a result of this study points to a need for a further in-depth examination into the kinetic, microphysical aspects of these evolving step-like switchback boundaries.

We gratefully acknowledge the dedication of the Parker Solar Probe project team that built such an enduring spacecraft. We also extend great thanks to the FIELDS and SWEAP instrument teams whose hard work and dedication created a very unique measurement set that will live on long after this exciting project is finished. Locally, at Goddard, we want to recognize the dedication of the magnetometer build team that was part of the FIELDS consortium and whose measurements we use herein. This work was funded by NASA via internal WBS as part of the Solar Probe project. The data set used to create the figures can be found on NASA's CDAWeb site (https://cdaweb.gsfc.nasa.gov/index.html/).

ORCID iDs

W. M. Farrell https://orcid.org/0000-0002-2284-7654
R. J. MacDowall https://orcid.org/0000-0003-3112-4201
S. D. Bale https://orcid.org/0000-0002-1989-3596
J. C. Kasper https://orcid.org/0000-0002-7077-930X

References

Bale, S. D., Badman, S. T., Bonnell, J. W., et al. 2019, Natur, 576, 237
Bale, S. D., Goetz, K., Harvey, P. R., et al. 2016, SSRv, 204, 49
Balogh, A., Forsyth, R. J., Lucek, E. A., et al. 1999, GeoRL, 26, 631
Chhiber, R., Goldstein, M. L., Maruca, B. A., et al. 2020, ApJ, 246, 31
Dudok de Wit, T., Krasnoselskikh, V. V., Bale, S. D., et al. 2020, ApJ, 246, 39
Farrell, W. M., Kaiser, M. L., & Steinberg, J. T. 1997, GeoRL, 24, 1135
Farrell, W. M., Kaiser, M. L., Steinberg, J. T., & Bale, S. D. 1998, JGR, 103, 23653
Fox, N. J., Velli, M. C., Bale, S. D., et al. 2016, SSRv, 204, 7
Horbury, T. S., Matteini, L., & Stansby, D. 2018, MNRAS, 478, 1980
Horbury, T. S., Woolley, T., Laker, R., et al. 2020, ApJ, 246, 45
Kasper, J. C., Abiad, R., Austin, G., et al. 2016, SSRv, 204, 131
Kasper, J. C., Bale, S. D., Belcher, J. W., et al. 2019, Natur, 576, 228
McComas, D. J., Alexander, N., Angold, N., et al. 2016, SSRv, 204, 187
Mozer, F. S., Agapitov, O. V., Bale, S. D., et al. 2020, ApJ, 246, 68
Ogilvie, K. W., Steinberg, J. T., Fitzenreiter, R. J., et al. 1996, GeoRL, 23, 1255
Phan, T. D., Bale, S. D., Eastwood, J. P., et al. 2020, ApJS, 246, 31
Squire, J., Chandran, B. D. G., & Meyrand, R. 2020, ApJL, 891, L2
Tenerani, A., Velli, M., Matteini, L., et al. 2020, ApJ, 246, 32
Vourlidas, A., Howard, R. A., Plunkett, S. P., et al. 2016, SSRv, 204, 83
Zhou, L.-L., Zank, G. P., Adhikari, L., et al. 2020, ApJS, 246, 26